








RESEARCH ARTICLE | JULY 11 2024

## Quantum emitters in aluminum nitride induced by heavy ion irradiation

Alexander Senichev ; Zachariah O. Martin ; Yongqiang Wang ; Owen M. Matthiessen; Alexei Lagutchev ; Han Htoon ; Alexandra Boltasseva ; Vladimir M. Shalaev 



APL Quantum 1, 036103 (2024)  
<https://doi.org/10.1063/5.0199647>



**APL Electronic Devices**  
Open, quality research for the broad electronics community

## Meet the new Editor-in-Chief



[Learn More](#)

# Quantum emitters in aluminum nitride induced by heavy ion irradiation

Cite as: APL Quantum 1, 036103 (2024); doi: 10.1063/5.0199647

Submitted: 23 January 2024 • Accepted: 23 June 2024 •

Published Online: 11 July 2024




View Online



Export Citation



CrossMark

Alexander Senichev,<sup>1,2,a)</sup>  Zachariah O. Martin,<sup>1,2</sup>  Yongqiang Wang,<sup>3</sup>  Owen M. Matthiessen,<sup>1</sup>  
Alexei Lagutchev,<sup>1</sup>  Han Htoon,<sup>2,4</sup>  Alexandra Boltasseva,<sup>1,2</sup>  and Vladimir M. Shalaev<sup>1,2,b)</sup> 

## AFFILIATIONS

<sup>1</sup>Elmore Family School of Electrical and Computer Engineering, Birck Nanotechnology Center and Purdue Quantum Science and Engineering Institute, Purdue University, 610 Purdue Mall, West Lafayette, Indiana 47907, USA

<sup>2</sup>Quantum Science Center, Department of Energy, A National Quantum Information Science Research Center of the U.S., Oak Ridge National Laboratory, 1 Bethel Valley Road, Oak Ridge, Tennessee 37830, USA

<sup>3</sup>Materials Science and Technology Division, Los Alamos National Laboratory, Los Alamos, New Mexico 87545, USA

<sup>4</sup>Materials Physics and Applications Division, Los Alamos National Laboratory, Los Alamos, New Mexico 87545, USA

<sup>a)</sup>Author to whom correspondence should be addressed: [senichev@purdue.edu](mailto:senichev@purdue.edu)

<sup>b)</sup>[shalaev@purdue.edu](mailto:shalaev@purdue.edu)

## ABSTRACT

The integration of solid-state single-photon sources with foundry-compatible photonic platforms is crucial for practical and scalable quantum photonic applications. This study explores aluminum nitride (AlN) as a material with properties highly suitable for integrated on-chip photonics and the ability to host defect-center related single-photon emitters. We have conducted a comprehensive analysis of the creation of single-photon emitters in AlN, utilizing heavy ion irradiation and thermal annealing techniques. Subsequently, we have performed a detailed analysis of their photophysical properties. Guided by theoretical predictions, we assessed the potential of Zirconium (Zr) ions to create optically addressable spin defects and employed Krypton (Kr) ions as an alternative to target lattice defects without inducing chemical doping effects. With a 532 nm excitation wavelength, we found that single-photon emitters induced by ion irradiation were primarily associated with vacancy-type defects in the AlN lattice for both Zr and Kr ions. The density of these emitters increased with ion fluence, and there was an optimal value that resulted in a high density of emitters with low AlN background fluorescence. Under a shorter excitation wavelength of 405 nm, Zr-irradiated AlN exhibited isolated point-like emitters with fluorescence in the spectral range theoretically predicted for spin-defects. However, similar defects emitting in the same spectral range were also observed in AlN irradiated with Kr ions as well as in as-grown AlN with intrinsic defects. This result is supportive of the earlier theoretical predictions, but at the same time highlights the difficulties in identifying the sought-after quantum emitters with interesting properties related to the incorporation of Zr ions into the AlN lattice by fluorescence alone. The results of this study largely contribute to the field of creating quantum emitters in AlN by ion irradiation and direct future studies emphasizing the need for spatially localized Zr implantation and testing for specific spin properties.

© 2024 Author(s). All article content, except where otherwise noted, is licensed under a Creative Commons Attribution-NonCommercial 4.0 International (CC BY-NC) license (<https://creativecommons.org/licenses/by-nc/4.0/>). <https://doi.org/10.1063/5.0199647>

## INTRODUCTION

Photonic platforms hold great potential for the realization of practical quantum technologies spanning communication, computing, and sensing.<sup>1-5</sup> Photons serve as excellent qubits for quantum networks, long-distance entanglement distribution, and quantum information processing due to their numerous degrees of freedom,

high propagation speed, and resistance to decoherence.<sup>6-8</sup> Photonic integrated circuits (PICs) with compact, controllable, and reconfigurable elements are crucial for the development of complex quantum systems.<sup>9-11</sup> On-chip incorporation of quantum light sources like single-photon emitters is a key to this integration.<sup>12,13</sup> Solid-state emitters offer reliable, potentially deterministic sources of single photons with high repetition rates and indistinguishability,

enabling quantum logical operations and entanglement distribution.<sup>14</sup> Importantly, quantum emitters in solids can provide the necessary interface between spin qubits and photons.<sup>15</sup>

Combining materials with single-photon emitters such as III-V quantum dots,<sup>16–18</sup> diamond,<sup>19,20</sup> hexagonal boron nitride,<sup>21–23</sup> and photonic platforms including silicon, silicon nitride, aluminum nitride (AlN), or lithium niobate<sup>24–26</sup> is currently accomplished predominantly by hybrid integration. However, there is a growing interest in alternative material platforms that can host both intrinsic high-purity single-photon sources and are compatible with wafer-scale growth and foundry fabrication processes. Such photonic platforms with intrinsic quantum emitters include silicon,<sup>27–29</sup> silicon carbide,<sup>30–32</sup> silicon nitride,<sup>33–35</sup> aluminum nitride,<sup>36–38</sup> and gallium nitride,<sup>39–41</sup> to name a few.

Among these platforms, aluminum nitride stands out for its unique properties, including compatibility with metal-oxide-semiconductor (CMOS) fabrication processes, wide-bandgap (6.2 eV), high refractive index (2.1), wide transparency window (from ultraviolet to mid-infrared), as well as second-order nonlinearity ( $\chi^{(2)} = 4.7$  pm/V),<sup>42</sup> though weaker compared to lithium niobate ( $\chi^{(2)} = 41.7$  pm/V).<sup>43</sup> AlN-based waveguides also exhibit moderately low losses of about 0.4 dB/cm around 1550 nm.<sup>44</sup> Even lower losses of  $\sim 1$  dB/m were achieved in Si<sub>3</sub>N<sub>4</sub>-based waveguides;<sup>45</sup> however, they suffer from strong autofluorescence in the visible spectral range, which is essentially absent in AlN.<sup>46</sup> Such autofluorescence can hinder the detection of single-photon emission from defects. The non-centrosymmetric wurtzite crystal structure of AlN possesses a piezoelectric property, which makes it suitable for microelectromechanical systems (MEMS).<sup>47</sup> AlN-based piezo-optomechanical actuators are demonstrated for cryogenic compatible programmable photonic circuits with high-speed phase modulation.<sup>48</sup> For more details on the properties of AlN for PICs, reviews<sup>46,47,49</sup> contain a comprehensive list of recent advances in on-chip AlN photonic devices. Finally, III-nitride semiconductors, including AlN, play a crucial role in solid-state lighting technology. They are second only to silicon within the microelectronics industry, benefiting from well-established growth processes and device fabrication techniques and facilities.

AlN has also attracted particular attention as a host of intrinsic point defects that act as single-photon sources.<sup>36–38,50</sup> Single-photon emitters in AlN were observed in as-grown samples fabricated by metal organic chemical vapor deposition.<sup>36</sup> The formation of quantum emitters has also been observed in AlN films after implantation with helium (He) ions and thermal annealing.<sup>38</sup> Recently, it was shown that femtosecond laser writing can be applied to create single quantum emitters in AlN crystals with a creation yield of  $>50\%$ .<sup>51</sup>

Despite the numerous single-photon emitters identified in AlN, none have yet demonstrated the ability to possess individually addressable spin properties. First-principles calculations suggest that AlN can indeed host spin defects, with Titanium (Ti) and Zirconium (Zr) transition-metal impurities.<sup>52,53</sup> These are predicted to form stable complexes with nitrogen vacancies, resulting in defects with spin-triplet ground states.<sup>52,53</sup> The incorporation of Zr species into AlN by ion implantation has been recently studied experimentally.<sup>54</sup> It was shown that Zr implantation into AlN induces an additional emission peak at 730 nm, attributed to Zr-based (Zr<sub>Al</sub>-V<sub>N</sub>)<sup>0</sup> defects. The previous structural analysis of Zr-implanted epitaxial

AlN films by Raman and x-ray absorption spectroscopies indicated that the dominant defects were substitutional impurities such as Zr<sub>Al</sub> or vacancies such as V<sub>Al</sub> and V<sub>N</sub>.<sup>55</sup> However, the single-photon properties of these defects remain unexplored.

In this study, we generated single-photon emitters in AlN through irradiation by heavy ions followed by thermal annealing. Zr ions were chosen to experimentally test the theoretically predicted creation of Zr-based quantum emitters with optically addressable spin properties. As a control, Kr ions were employed to create quantum emitters based on crystal-lattice defects without inducing chemical doping for comparison with Zr-irradiated samples. A broad ion beam irradiation was applied to simplify the search for emitters and assess their density. We systematically varied the ion irradiation fluences to obtain the desired density of emitters without causing drastic damage to the crystal lattice.

Our results show that under 532 nm excitation, the observed single-photon emitters are primarily associated with vacancy or interstitial-type defects in the AlN lattice induced by ion irradiation, applicable to both Zr and Kr ions, without their incorporation. We observed a broad spectral distribution of emission from individual single-photon sources, including the appearance of narrow emission peaks at room temperature, as compared to emitters created in He-implanted AlN.<sup>38</sup> Furthermore, under a shorter wavelength excitation at 405 nm, Zr-irradiated films exhibited isolated point-like defects emitting in the spectral range associated with theoretically predicted Zr-based spin defects. However, isolated emitters in this spectral range were also detected in Kr-irradiated and control as-grown samples, which contain only intrinsic defects, complicating the definitive identification of Zr-based emitters using only spectroscopic techniques. This work sets the stage for further experiments to verify the correlation of these single-photon emitters with the incorporation of Zr ions into the AlN lattice and to explore their spin properties.

## EXPERIMENTAL

For this study, we used commercially available crystalline 200-nm-thick AlN films grown on sapphire (refer to Methods for detailed information). The fabrication process of quantum emitters by heavy ion implantation is illustrated in Fig. 1(a). Prior to ion implantation and thermal annealing, the 2-in. AlN-on-Sapphire wafers were diced into 10 × 10 mm<sup>2</sup> samples. Photoluminescence intensity maps of as-grown AlN samples recorded before ion implantation show low background fluorescence and the absence of isolated emitters [Fig. 1(d)]. Two groups of samples were implanted with <sup>90</sup>Zr<sup>+</sup> ions at an implantation energy of 200 keV and <sup>84</sup>Kr<sup>+</sup> ions at 190 keV, respectively. The implantation energy was chosen using Stopping and Range of Ions in Matter (SRIM) simulations to obtain an implantation depth of  $\sim 100$  nm or less [Fig. 1(b)]. The implantation energies were kept the same for all the implanted samples. The implantation fluence was systematically varied to assess its influence on the formation of single-photon emitters. We selected four ion fluences detailed in Table 1, which cover the available range of the 200 kV Danfysik Research Ion Implanter (see Methods for details).

The as-grown sample A, Zr-implanted samples B-E, and Kr-implanted samples F-I were annealed under the same conditions: at 1000 °C for 30 min in an argon atmosphere [Fig. 1(c)]. The thermal

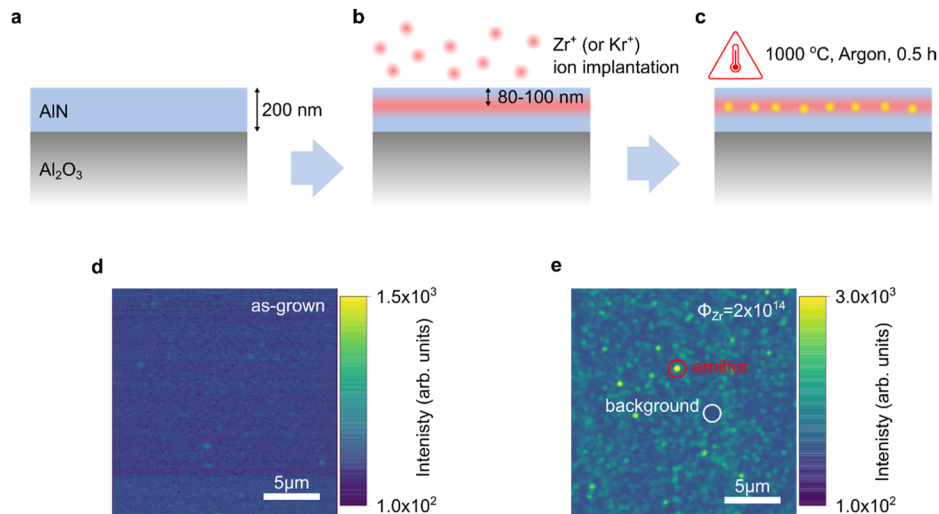


**FIG. 1.** Fabrication process of single-photon emitters in AlN by heavy ion implantation using Zr and Kr: (a) As-grown 200-nm-thick AlN film on sapphire grown by a plasma vapor deposition nanocolumnar process (Kyma Technologies Inc.); (b) Zr and Kr ion implantation with an acceleration voltage of 200 and 190 keV, respectively, for the target implantation depth of about 80–100 nm; (c) Annealing of ion-implanted AlN films at 1000 °C in argon ambience for 30 min for creation of photostable single-photon emitters. (d) PL intensity map of an as-grown AlN sample without thermal annealing. (e) PL intensity map of a representative AlN film implanted at a Zr-ion fluence of  $\Phi_{\text{Zr}} = 2 \times 10^{14}$  (sample D) and annealed at 1000 °C in an argon atmosphere for 30 min. Red circle: representative single-photon emitter; white circle: typical area with no emitters for AlN background emission measurements.

**TABLE I.** List of samples with applicable implantation and thermal annealing conditions.

Sample no.	Implantation species	Implantation energy	Ion fluence $\Phi_{\text{Zr}}$ (ions/cm <sup>2</sup> )	Thermal annealing
A	Control sample without implantation			
B			$5 \times 10^{11}$	
C	<sup>90</sup> Zr <sup>+</sup>	200 keV	$1 \times 10^{13}$	T = 1000 °C argon 30 min
D			$2 \times 10^{14}$	
E			$2 \times 10^{15}$	
F		$6 \times 10^{11}$		
G	<sup>84</sup> Kr <sup>+</sup>	190 keV	$1 \times 10^{13}$	
H			$2 \times 10^{14}$	
I			$2 \times 10^{15}$	

annealing step was performed to repair the lattice damage introduced by ion implantation and to activate single-photon emitters [Fig. 1(e)].

## RESULTS AND DISCUSSION

### Emergence of single-photon emitters in ion-implanted AlN films

First, we examine the density of single-photon emitters in AlN following thermal annealing as a function of the ion implantation fluence. We focus on the results from Zr-implanted AlN samples dis-

cussed in the main paper. [Supplementary material](#) details the results from Kr-implanted samples, providing a reference for a comparative analysis.

In search of single-photon emitters in AlN films, we employed a 532 nm laser, commonly used for studying quantum emitters in the visible range. We found that subsequent annealing of the as-grown control sample A without implantation resulted in sparse isolated bright spots, as evidenced in photoluminescence (PL) intensity maps [Fig. 2(a)]. These were confirmed to be single-photon emitters by second-order autocorrelation measurements. Our observations agree with earlier findings in the literature, suggesting that as-grown AlN films may contain intrinsic point defects capable of acting as single-photon emitters.<sup>36,37</sup> The PL spectrum and the

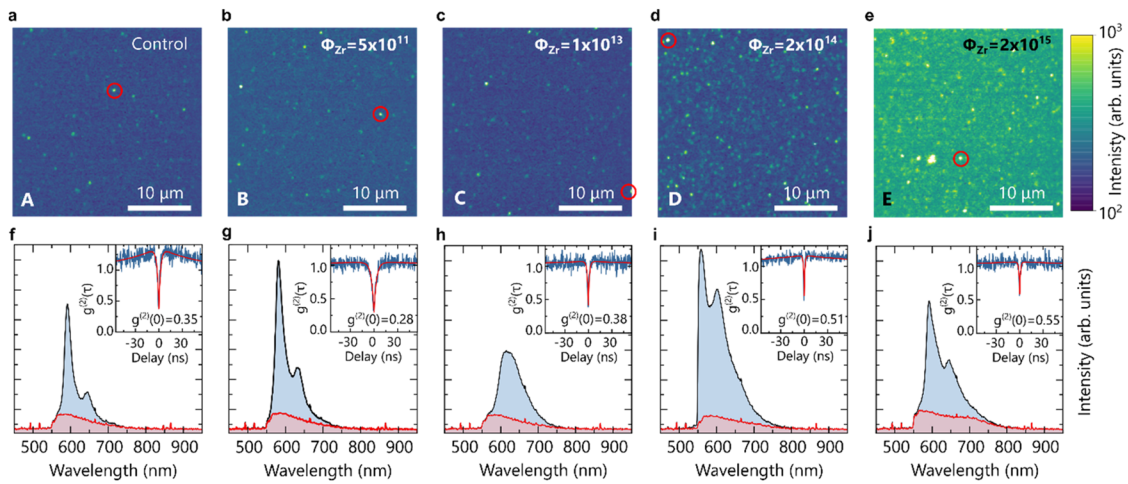


**FIG. 2.** Confocal  $30 \times 30 \mu\text{m}^2$  PL intensity maps for different Zr-implanted AlN samples with an implantation fluence: (a) as-grown control sample, (b)  $\Phi_{\text{Zr}} = 5 \times 10^{11}$ , (c)  $\Phi_{\text{Zr}} = 1 \times 10^{13}$ , (d)  $\Phi_{\text{Zr}} = 2 \times 10^{14}$ , (e)  $\Phi_{\text{Zr}} = 2 \times 10^{15}$ . [(f)–(j), in blue]: PL spectra of representative emitters indicated in PL intensity maps (a)–(e) with red circles. [(f)–(j), in red]: background PL spectra of AlN film in the areas without emitters. Insets: second-order autocorrelation histograms  $g^{(2)}(\tau)$  fitted with a three-level model.

second-order autocorrelation histogram of a representative quantum emitter from the as-grown annealed AlN sample (A) are shown in Fig. 2(f). A typical PL spectrum from one of these emitters consists of a pronounced emission peak and a red-shifted broad emission attributed to the zero-phonon line (ZPL) and phonon sideband (PSB), respectively. The PL intensity of emitters is substantially stronger than background PL, as can be seen from the comparison of two corresponding spectra [Fig. 2(f) blue and red curves, respectively]. Fitting of the second-order autocorrelation histogram yields a  $g^{(2)}(0)$  value of 0.35 without background correction or spectral filtering.

Next, we analyze the properties of single-photon emitters created by Zr ion irradiation. We found that the density of emitters changes as a function of the ion implantation fluence [Figs. 2(b)–2(e)]. The density of the isolated emitters remains virtually the same for the two lowest ion fluences of  $5 \times 10^{11}$  ions/cm<sup>2</sup> (sample B) and  $1 \times 10^{13}$  ions/cm<sup>2</sup> (sample C) and is comparable to the as-grown control sample (A) after annealing [Figs. 2(a)–2(c)]. However, the single-photon emitter density increases by at least a factor of two for the implantation fluence of  $2 \times 10^{14}$  ions/cm<sup>2</sup> (sample D) compared to the control sample (A). Details on the quantitative analysis of emitter density are provided in the [supplementary material](#) (Fig. S1). Further increases in the implantation fluence to  $2 \times 10^{15}$  ions/cm<sup>2</sup> (sample E) do not substantially change the density of emitters but dramatically increase the background fluorescence of the AlN film itself. Hence, the ion fluence of  $2 \times 10^{14}$  ions/cm<sup>2</sup> or near its vicinity appeared to be optimal for creating emitters with high surface density while simultaneously keeping the AlN background fluorescence close to the level of as-grown AlN.

The PL spectra of representative single-photon emitters in AlN for four implantation fluences are shown in Figs. 2(g)–2(j). The PL spectrum structure of individual emitters resembles the one

observed in control sample A, with a pronounced ZPL peak accompanied by lower energy sidebands, PSBs. The room-temperature ZPL linewidth varies among different emitters, which may be related to different implantation conditions, but establishing a correlation will require further analysis. The typical  $g^{(2)}(\tau)$  values at zero delay time  $\tau = 0$  registered without spectral filtering or background correction were typically below or about 0.5, confirming the single-photon nature of the emitters [insets of Figs. 2(g)–2(j)]. The decrease in single-photon purity with the increase in implantation fluence to  $2 \times 10^{15}$  ions/cm<sup>2</sup> may be attributed to the increased background fluorescence of the AlN films [Fig. 2(j), inset].

The investigation into Kr-implanted AlN films reveals a comparable correlation between the formation of single-photon emitters and implantation fluence, resulting in increased emitter density and elevated background fluorescence as the fluence increases (Fig. S2, [supplementary material](#)). Notably, the background intensity seems lower for Kr-implanted AlN films in comparison to the Zr-implanted samples, which we will discuss later.

Along with typical PL emission spectra presented in Figs. 2(g)–2(j), occasionally PL spectra with different features, like a single broad peak or multiple peaks of varying widths and relative intensities, were also observed (Fig. S3, [supplementary material](#)). These less common spectra may result from the interaction of quantum emitters with the surrounding AlN lattice, the presence of multiple emitters within the excitation spot, or the existence of additional defect complexes associated with various point-like defects, including vacancies, substitutions, or impurities. Notably, these spectra differ from previously reported ones for quantum emitters in as-grown AlN with a relatively weak ZPL transition and an intensely broad phonon sideband.<sup>37</sup> Furthermore, certain AlN defects created by our method produce emission peaks with narrower line widths as compared to those reported for He-implanted AlN defects at room temperature.<sup>38</sup>

## Spectral properties of the photoluminescence from AlN single-photon emitters

We now turn to a comparative analysis, aiming to differentiate between pre-existing defects in as-grown sample A and those induced by ion implantation in both Zr-irradiated (B–E) and subsequently Kr-irradiated AlN (F–I). For ion-irradiated samples, we focus on the sample with the optimal implantation fluence  $\Phi_{\text{Zr}} = 2 \times 10^{14}$  (D), which exhibited the highest emitter density and minimal AlN background fluorescence.

We analyzed the distribution of ZPL wavelength for the control and ion irradiated samples [Figs. 3(a) and 3(d)]. For this purpose, we identified single-photon emitters with  $g^{(2)}(0) < 0.5$  [Figs. 3(c) and 3(f)] and recorded the wavelength of the most intense peak per spectrum, attributed to the ZPL transition. This analysis shows similar median values of the ZPL peak position: 592 and 590 nm for the control (A) and irradiated sample (D), respectively. Both histograms reveal the most frequent value for ZPL at 585 nm. Interestingly, the ZPL histogram peak at this spectral position was also reported for MOCVD-grown AlN films.<sup>36</sup> In addition, a possibly less pronounced peak at roughly 630 nm was resolved in our histograms.

Representative PL spectra of emitters from the spectral regions indicated with dashed lines in Figs. 3(a) and 3(d) for as-grown and Zr-irradiated samples are shown in Figs. 3(b) and 3(e). The room-temperature ZPL linewidth, assessed using the Lorentzian line shape, ranges from 8 to 17 nm. Sample D implanted with  $\Phi_{\text{Zr}} = 2 \times 10^{14}$  also shows similar PL spectra with ZPL linewidths spanning 9–24 nm, not significantly wider than emitters in the as-grown AlN.

The wavelength distribution of the most intense peak in the PL spectra of Kr-irradiated samples is shown in Fig. S4, supplementary

material, and follows similar behavior as for control and Zr-irradiated samples. This points to the possibility that defects created in both samples are of similar nature. It appears that both Zr and Kr ions were likely to induce damage to the AlN lattice and form vacancy-type defects rather than becoming chemically bonded to it.

In addition to room-temperature measurements, we performed PL spectra measurements of Zr-irradiated samples at cryogenic temperatures. At liquid-nitrogen temperatures, the single-photon emitters exhibited substantially narrower ZPL linewidths, down to about 4 nm. Moreover, the emission was found to predominantly occur through the ZPL transitions. We estimated the Debye–Waller factor to be about 22%, 43%, and 62% for the PL spectra of SPE1, SPE2, and SPE3 emitters shown in Fig. 4(a), respectively.

Analyzing the single-photon purity of AlN quantum emitters at room temperature [Figs. 3(c) and 3(f)], we found that the  $g^{(2)}(0)$  histogram from the as-grown sample A shows a distribution with a median value of 0.54. In Zr-implanted sample D, a substantial number of emitters exhibited  $g^{(2)}(0)$  values below 0.5, although the median value of the respective distribution is 0.65. A similar trend is observed for emitters in Kr-implanted samples (Fig. S4, supplementary material). This can be attributed to the presence of ion-induced emitters in the implanted samples that differ from those in the as-grown samples. The reduced  $g^{(2)}(0)$  values are due to either the defect structure itself or an increased background emission rate.

## Polarization analysis of emission

We measured PL intensity maps from the Zr-implanted sample D for various orientations of the polarizer in front of the detector,

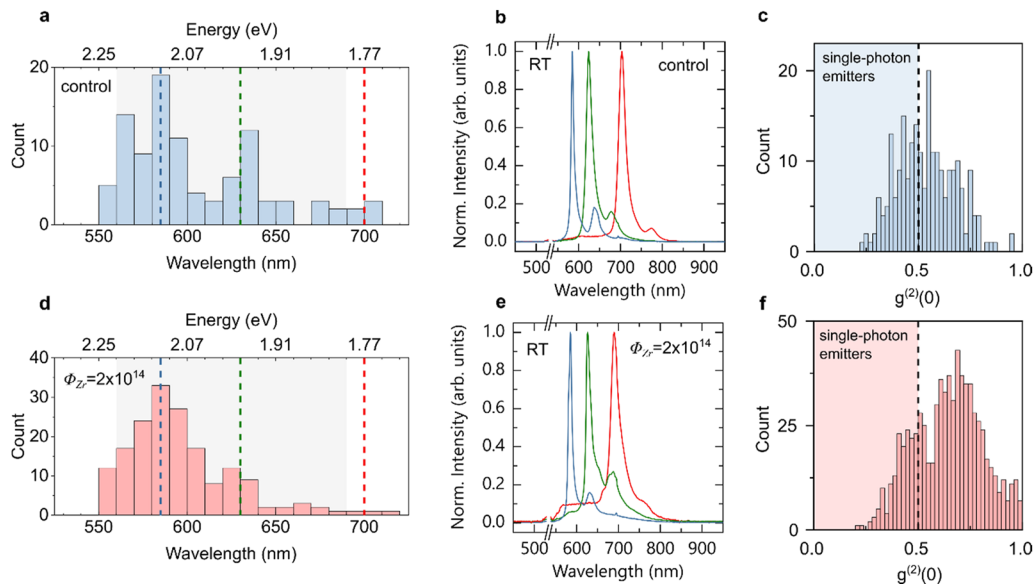


**FIG. 3.** (a) and (d) ZPL peak wavelength distribution obtained from 102 to 174 single-photon emitters with  $g^{(2)}(0) < 0.5$  in the control (A) and Zr-irradiated (D) samples, respectively; bin size 10 nm. (b) and (e) Representative normalized PL spectra for the spectral regions indicated in (a) and (d). (c) and (f) Histograms of  $g^{(2)}(0)$  distribution for emitters in samples A (238 emitters) and D (745 emitters); bin size 0.02. The  $g^{(2)}(0)$  values were obtained without background correction and spectral filtering.

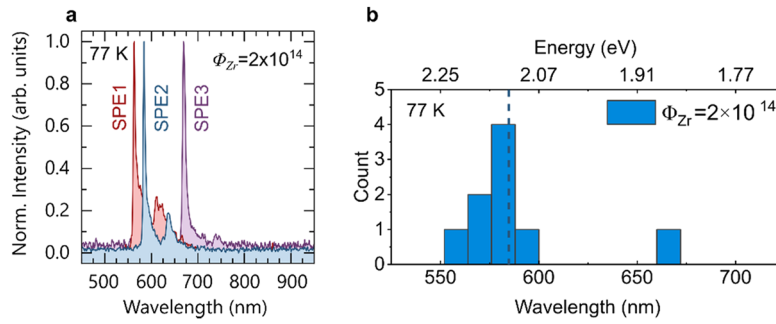


**FIG. 4.** Low-temperature (77 K) photoluminescence spectroscopy of single-photon emitters in Zr-irradiated AlN (D). (a) Three representative normalized PL spectra with ZPL wavelengths of SPE<sub>1</sub> (563 nm), SPE<sub>2</sub> (584 nm), and SPE<sub>3</sub> (669 nm). (b) ZPL wavelength distribution for nine PL spectra measured at 77 K with the mean value of  $588 \pm 32$  nm, dashed line; bin size 12 nm.

e.g., Fig. 5(a) at 0°. The map of the difference between PL intensities measured at 0° and 90° allowed us to identify emitters with different emission polarizations [Fig. 5(b)]. Additional maps of the difference between PL intensities measured at different orientations of the polarizer are shown in [supplementary material](#), Fig. S5. The

polarization diagrams in Figs. 5(c) and 5(d) show quantum emitters with mutually orthogonal polarization states, consistent with previously reported emitters in He-implanted AlN samples.<sup>38</sup> Moreover, we observed emitters with varied PL polarization [Fig. 5(e)], suggesting the presence of various emitter orientations. The PL spectra of

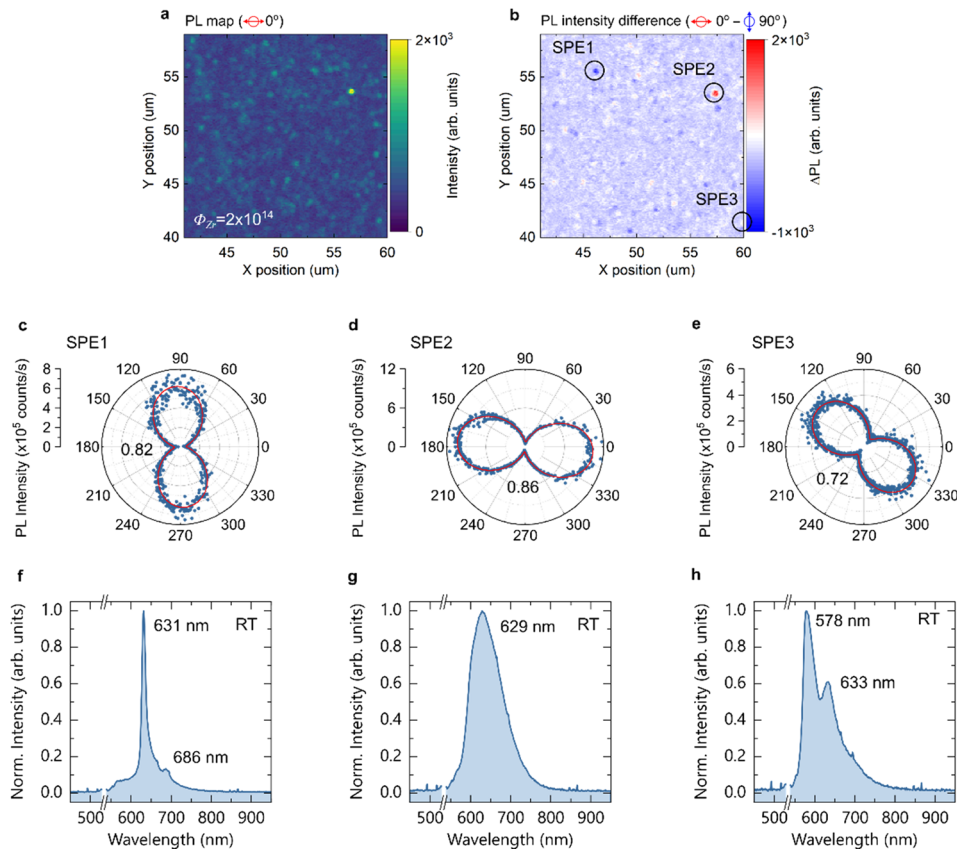


**FIG. 5.** Polarization analysis of PL emission. (a) Confocal  $20 \times 20 \mu\text{m}^2$  PL intensity map of the Zr-implanted sample D measured at 0° of the polarizer. (b) PL intensity map produced by subtraction of PL intensity maps collected at 90° from the one at 0° of the polarizer rotation. (c)–(e) Polarization diagrams depicting the PL emission from emitters labeled in (b) with (f)–(h) corresponding PL spectra.

these emitters are shown in Figs. 5(f)–5(h). Further investigating the correlation between crystalline structure orientation and the polarization of the photoluminescence requires in-depth analysis beyond the scope of this study. Such a future study could uncover emitter classes and corresponding defects correlated with crystallographic directions in AlN films.

### Search for Zr-related defects at shorter wavelengths

The experiments conducted with 532 nm laser excitation did not conclusively demonstrate the formation of single-photon emitters involving Zr-incorporated defects. The heavy ion irradiation introduces various types of lattice defects which, along with as-grown defects, complicate the identification of emitters specifically related to the incorporation of Zr ions into the AlN lattice or other impurity-related defects. In addition to PL spectra from individual single-photon emitters, we measured using the 532 nm excitation wavelength the background fluorescence of AlN films away from emitters and found the dependence on implantation fluence

(Fig. S6, supplementary material). We found the appearance of the strong PL band at about 700 nm with the increase of the irradiation fluence (Fig. S6b). Notably, this PL peak is more pronounced for Zr-irradiated AlN samples compared to the Kr-irradiated samples. The rise of an additional PL band and the increase in its intensity with ion irradiation fluence may indicate the formation of Zr-based defects in addition to vacancy-type defects due to ion irradiation induced damage to the AlN lattice. Interestingly, an additional emission in bulk AlN films implanted with Zr ions at 730 nm (1.7 eV) has been previously observed using a laser source at 266 nm.<sup>54</sup> This emission line was attributed to the formation of Zr-related defect complexes. However, the formation of single-photon emitters was not addressed in that study.

In the work by Varley *et al.*, it was predicted from the first-principles calculations based on density functional theory (DFT) that for the Zr-related defect complex such as  $(\text{Zr}_{\text{Al}}\text{V}_{\text{N}})^0$ , the ZPL transition should occur at 2.36 eV, or 525 nm.<sup>52</sup> To explore quantum emitters with PL emission at this specific wavelength, we employed a shorter wavelength excitation at 405 nm. We found that the back-

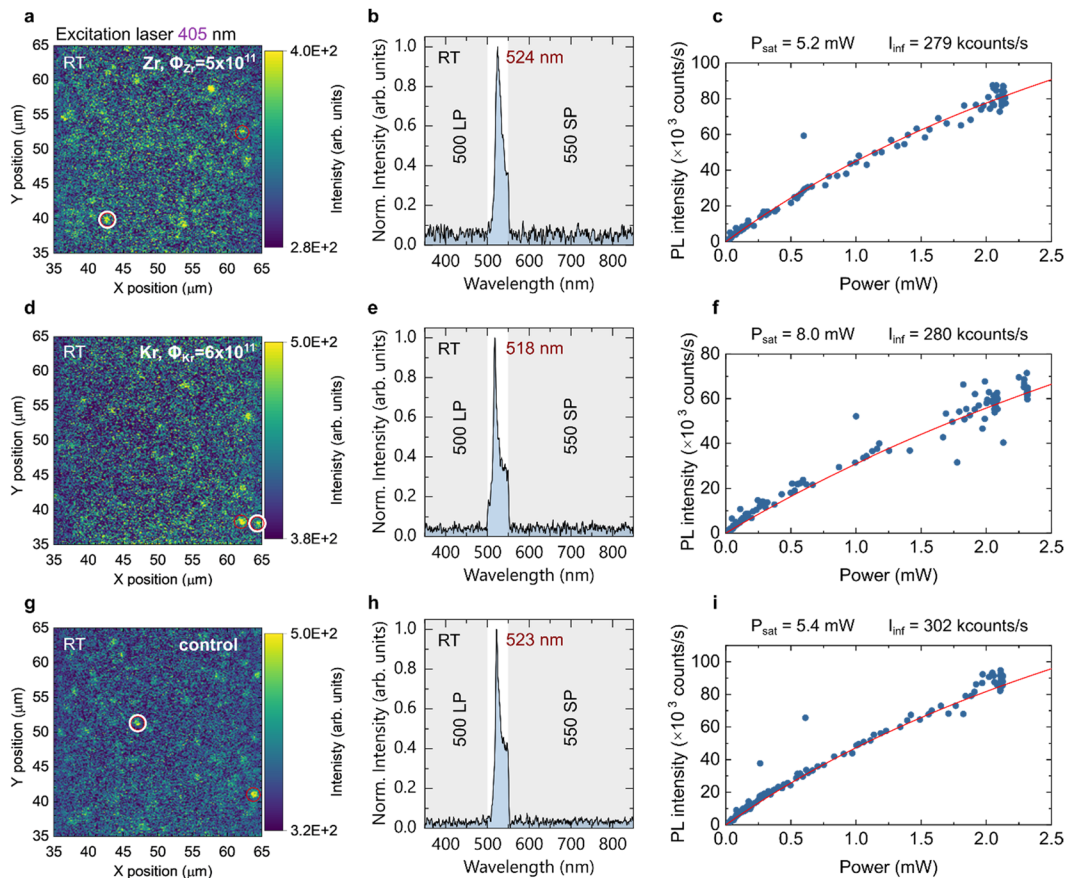


**FIG. 6.** Analysis of single-photon emitters at short wavelengths using 405 nm excitation at room temperature. Confocal  $30 \times 30 \mu\text{m}^2$  PL intensity maps with representative emitters marked by white circles, the PL spectrum of the indicated emitters, and the corresponding power saturation curves (blue dots) fitted theoretically (red line). Each set of panels corresponds to different sample conditions: (a)–(c) Zr-irradiated AlN with  $\Phi_{\text{Zr}} = 5 \times 10^{11}$  ions/cm<sup>2</sup>, (d)–(f) Kr-irradiated AlN with  $\Phi_{\text{Kr}} = 6 \times 10^{11}$  ions/cm<sup>2</sup>, and (g)–(i) control AlN sample without ion irradiation. Emission was filtered using a 500 nm long-wavelength pass and a 550 nm short-wavelength pass filter to isolate the spectral region associated with predicted spin defects. Both PL spectra and saturation curves have been background corrected.



ground PL intensity under this excitation wavelength is substantially stronger than with the 532 nm laser, even for the lowest ion implantation fluence. Despite the strong background PL, we were able to identify isolated bright spots in samples with the lowest implantation fluences of  $\Phi_{\text{Zr}} = 5 \times 10^{11}$  and  $\Phi_{\text{Kr}} = 6 \times 10^{11}$  ions/cm<sup>2</sup>, as shown in Fig. 6. We used both long-pass and short-pass filters that allowed measurements only in the spectral range of 500–550 nm. This enabled us to detect isolated bright spots that displayed distinct PL spectra from the AlN background. Most notably, we identified emitters with a PL peak positioned around 525 nm, where emission from Zr-related defects is expected [Figs. 6(a) and 6(b)]. However, the low signal-to-noise ratio presented challenges in measuring the second-order autocorrelation histograms necessary to confirm the single-photon nature of these emitters. Consequently, our future study will require a slightly longer excitation wavelength, closer to the ZPL transition at 525 nm. We also conducted power-dependent PL intensity measurements and observed a saturation effect at reasonable power levels and maximum intensity values [Fig. 6(c)]. This behavior suggests that the emission originates from localized defects with a finite density of states, characteristic of single-photon emitters.

While we identified bright spots with a PL peak around 525 nm in Zr-irradiated samples, similar emission was also detected in Kr-irradiated [Figs. 6(d)–6(f)] and control as-grown samples, which contain only intrinsic defects [Figs. 6(g)–6(i)]. It is likely that various defect types in AlN, both induced by heavy ion irradiation and naturally present, contribute to a broad spectral distribution of single-photon emitters. This complexity hinders the identification of specific defects that may exhibit unique spin properties using only PL spectroscopy techniques. To identify Zr-related defects, future studies should employ site-controlled focused ion beam implantation and additional techniques to directly probe the spin properties of newly formed defects, which are beyond the scope of this work.

Interestingly, the change in excitation wavelength led to a noticeable non-monotonic dependency of the AlN background fluorescence on the Zr and Kr ion irradiation fluence, as detailed in the [supplementary material](#) (Fig. S7). The background PL intensity increases up to a Zr ion fluence of  $\Phi_{\text{Zr}} = 2 \times 10^{14}$  ions/cm<sup>2</sup> and then decreases at  $\Phi_{\text{Zr}} = 2 \times 10^{15}$  ions/cm<sup>2</sup>. This behavior contrasts with the response under 532 nm excitation, where higher fluences lead to increased PL intensity. Under 405 nm excitation, the PL peak initially shifts to longer wavelengths before decreasing at higher fluences. This may suggest a buildup of strain from defect accumulation and subsequent relaxation.<sup>56</sup> The observed reduction in background intensity in this spectral range at higher fluences is likely due to the creation of additional non-radiative decay channels. For more details, refer to the [supplementary material](#) (Fig. S7).

## CONCLUSION

In conclusion, this study provided a comprehensive analysis of single-photon emitters in AlN induced by Zr and Kr heavy ion irradiation, followed by thermal annealing. Our results showed that ion irradiation is an effective method for creating single-photon emitters in the AlN lattice for both types of ions. Under 532 nm excitation, the observed single-photon emitters in the irradiated samples displayed characteristics similar to those of sparse emitters in non-irradiated samples. The results of Zr and Kr irradiation

showed similar outcomes, suggesting that these emitters may be formed without the incorporation of these ions into the lattice, primarily associated with point defects such as vacancies or interstitial defects. We observed that the density of emitters increased with ion fluence, with an optimal balance between emitter density and AlN background fluorescence achieved at  $\Phi_{\text{Zr}} = 2 \times 10^{14}$ . Under 405 nm excitation, Zr-irradiated AlN exhibited unique spectral properties, possibly indicating the presence of theoretically predicted optically active Zr-based defect complexes. However, emitters in this spectral range were also detected in Kr-irradiated and control samples, complicating the identification of defects associated with Zr incorporation using only fluorescence spectroscopy. Future investigations should focus on exploring the single-photon emission and spin properties of these defects, particularly to resolve Zr-based emitters, to unlock their potential in quantum technologies. This research enhances our understanding of defect-related single-photon emitters in AlN and advances the AlN platform for quantum photonic applications.

## METHODS

### Formation of emitters by implantation and thermal annealing

We used commercially available AlN templates on sapphire (Al<sub>2</sub>O<sub>3</sub>) substrates grown by plasma vapor deposition of nanocolumns (PVDNC<sup>TM</sup>) from Kyma Technologies Inc. The nominal AlN film thickness was 200 nm ± 5%. The 2 in. wafer was diced into 10 × 10 mm<sup>2</sup> samples for subsequent ion implantation.

The implantation was performed on a 200 kV Danfysik Research Ion Implanter in the Ion Beam Materials Laboratory at Los Alamos National Laboratory (LANL). The implantation energy of 200 keV (190 keV) was selected to restrict the Zr (Kr) implantation depth to ~80 nm following the simulation results obtained with Stopping and Range of Ions in Matter (SRIM) software. We used the ion fluence from  $\Phi_{\text{Zr}} = 5 \times 10^{11}$  to  $\Phi_{\text{Zr}} = 2 \times 10^{15}$  to vary the concentration of Zr or Kr ion incorporation. The target temperature was kept at room temperature during all implantations.

The samples were then solvent cleaned and annealed in a conventional quartz tube furnace (Blue M Oven Furnace) at 1000 °C under an argon (Ar) atmosphere for 30 minutes. After thermal annealing, the samples were cleaned with solvents and plasma washed with O<sub>2</sub> gas. The formation of single-photon emitters was confirmed then by photoluminescence intensity mapping.

### Experimental setup

The optical characterization of quantum emitters in AlN samples was conducted at both room temperature and liquid nitrogen (77 K) using the freezing microscope stage (THMS600, Linkam). We utilized a custom-built scanning confocal microscope, which was based on a commercially available inverted microscope body (Nikon, Ti-U model). This microscope was equipped with a 100 μm pinhole and a 100× air objective featuring a numerical aperture (NA) of 0.90, all provided by Nikon. For measurements at liquid-nitrogen temperatures, we used a 50× air objective with an NA of 0.60 (Nikon). To facilitate confocal scanning, the objective was mounted on a piezo stage, specifically the Physik Instrumente P-561 model, controlled by a Physik Instrumente E-712 controller, and

interfaced with LabVIEW from National Instruments. For optical excitation of the emitters, we employed a continuous wave diode-pumped solid-state laser with a power output of 200 mW, emitting at 532 nm (Lambda beam PB 532-200 DPSS, RGB Photonics). The laser pump spot size on the sample was estimated to be  $\sim 1 \mu\text{m}$ . To separate the excitation light from the photoluminescence (PL) signal, we utilized a 550 nm long-pass dichroic mirror (DMLP550, Thorlabs). Any residual pump power was further attenuated using a 550 nm long-pass filter (FEL0550, Thorlabs) positioned in front of the detectors. For short-wavelength excitation, we used a continuous-wave diode laser emitting at 405 nm with an output power of 200 mW (Lambda beam PB 405-200, RGB Photonics). The laser light was filtered from the PL signal using a 409 nm long-pass filter (FF02-409/LP-25, AVR Optics). Emission data were collected using an avalanche detector with a quantum efficiency of 69% at 650 nm (SPCM-AQRH, Excelitas) to enable single-photon detection during the scanning process. To investigate the quantum characteristics of the emitters, we conducted measurements of the second-order autocorrelation function  $g^{(2)}(\tau)$  employing a Hanbury Brown and Twiss (HBT) setup. This setup consisted of two avalanche detectors featuring a time resolution of 30 ps and a quantum efficiency of 35% at 650 nm (PDM, Micro-Photon Devices), along with an acquisition card featuring just 4 ps internal jitter (SPC-150, Becker and Hickl).

## NOTES

While preparing this paper, the authors learned about another study that describes single-photon emitters in aluminum nitride, created through the process of aluminum ion implantation, as referenced in Ref. 57.

## SUPPLEMENTARY MATERIAL

The [supplementary material](#) provides details on the quantification of the density of single-photon emitters, PL data, and analysis for AlN samples implanted with Zr and Kr ions. It includes various PL intensity maps for Kr-implanted samples across different ion fluences with corresponding PL spectra and second-order autocorrelation histograms. It also features additional room-temperature PL spectra from Zr-implanted samples, illustrating emitter characteristics such as linewidth and wavelength of emission lines. Data on ZPL peak wavelength distribution from Kr-implanted samples, including histograms of  $g^{(2)}(0)$  values, are presented. Additionally, polarization-dependent intensity maps for the Zr-implanted sample highlight differences in emission due to polarizer orientation. Detailed examinations of background PL spectra for both Zr and Kr implanted samples at various fluences showcase changes in emission intensity and the emergence of new PL bands, particularly around 700 nm. The [supplementary material](#) also includes background fluorescence intensity analyses as a function of ion fluence, specifically noting changes in Zr and Kr-implanted samples under 405 nm excitation, aiding in understanding the effects of heavy ion implantation on the formation and characteristics of single-photon emitters in AlN.

## ACKNOWLEDGMENTS

This work was supported by the U.S. Department of Energy (DOE), the Office of Science through the Quantum Science Center

(QSC), the National Science Foundation Award No. 2015025-ECCS, and the Air Force Office of Scientific Research (AFOSR) grant FA9550-22-1-0372. Zr and Kr ion implantation is supported by the DOE BES grant, LANLE3QR, and performed at the Center for Integrated Nanotechnologies (CINT), an Office of Science User Facility operated for the U.S. Department of Energy (DOE) Office of Science by Los Alamos National Laboratory. Los Alamos National Laboratory, an affirmative action equal opportunity employer, is managed by Triad National Security, LLC, for the U.S. Department of Energy's NNSA under Contract No. 89233218CNA000001.

## AUTHOR DECLARATIONS

### Conflict of Interest

The authors have no conflicts to disclose.

### Author Contributions

**Alexander Senichev:** Conceptualization (equal); Data curation (equal); Formal analysis (equal); Investigation (equal); Writing – original draft (equal); Writing – review & editing (equal). **Zachariah O. Martin:** Formal analysis (equal); Investigation (equal); Writing – review & editing (equal). **Yongqiang Wang:** Investigation (equal); Resources (equal); Writing – review & editing (equal). **Owen M. Matthiessen:** Investigation (equal); Writing – review & editing (equal). **Alexei Lagutchev:** Methodology (equal); Resources (equal); Writing – review & editing (equal). **Han Htoon:** Conceptualization (equal); Investigation (equal); Supervision (equal); Writing – review & editing (equal). **Alexandra Boltasseva:** Funding acquisition (equal); Supervision (equal); Writing – review & editing (equal). **Vladimir M. Shalaev:** Conceptualization (equal); Funding acquisition (equal); Project administration (equal); Resources (equal); Supervision (equal); Writing – review & editing (equal).

## DATA AVAILABILITY

The data that support the findings of this study are available within the article and its [supplementary material](#).

## REFERENCES

- 1 J. L. O'Brien, "Optical quantum computing," *Science* **318**, 1567 (2007).
- 2 A. Aspuru-Guzik and P. Walther, "Photonic quantum simulators," *Nat. Phys.* **8**, 285 (2012).
- 3 H. J. Kimble, "The quantum internet," *Nature* **453**, 1023 (2008).
- 4 S. Wehner, D. Elkouss, and R. Hanson, "Quantum internet: A vision for the road ahead," *Science* **362**, eaam9288 (2018).
- 5 C. L. Degen, F. Reinhard, and P. Cappellaro, "Quantum sensing," *Rev. Mod. Phys.* **89**, 035002 (2017).
- 6 F. Flamini, N. Spagnolo, and F. Sciarrino, "Photonic quantum information processing: A review," *Rep. Prog. Phys.* **82**, 016001 (2019).
- 7 M. Pompili *et al.*, "Realization of a multinode quantum network of remote solid-state qubits," *Science* **372**, 259 (2021).
- 8 Y.-A. A. Chen *et al.*, "An integrated space-to-ground quantum communication network over 4,600 kilometres," *Nature* **589**, 214 (2021).
- 9 A. Politi, J. Matthews, M. G. Thompson, and J. L. O'Brien, "Integrated quantum photonics," *IEEE J. Sel. Top. Quantum Electron.* **15**, 1673 (2009).
- 10 L. S. Madsen *et al.*, "Quantum computational advantage with a programmable photonic processor," *Nature* **606**, 75 (2022).

- <sup>11</sup>G. Moody *et al.*, “2022 Roadmap on integrated quantum photonics,” *J. Phys.: Photonics* **4**, 012501 (2022).
- <sup>12</sup>J. Lee, V. Leong, D. Kalashnikov, J. Dai, A. Gandhi, and L. A. Krivitsky, “Integrated single photon emitters,” *AVS Quantum Sci.* **2**, 031701 (2020).
- <sup>13</sup>M. Sasani Ghamsari, “Chip-scale quantum emitters,” *Quantum Rep.* **3**, 615 (2021).
- <sup>14</sup>I. Aharonovich, D. Englund, and M. Toth, “Solid-state single-photon emitters,” *Nat. Photonics* **10**, 631 (2016).
- <sup>15</sup>D. D. Awschalom, R. Hanson, J. Wrachtrup, and B. B. Zhou, “Quantum technologies with optically interfaced solid-state spins,” *Nat. Photonics* **12**, 516 (2018).
- <sup>16</sup>J.-H. Kim, S. Aghaeimeibodi, C. J. K. Richardson, R. P. Leavitt, D. Englund, and E. Waks, “Hybrid integration of solid-state quantum emitters on a silicon photonic chip,” *Nano Lett.* **17**, 7394 (2017).
- <sup>17</sup>M. Davanco, J. Liu, L. Sapienza, C.-Z. Zhang, J. V. De Miranda Cardoso, V. Verma, R. Mirin, S. W. Nam, L. Liu, and K. Srinivasan, “Heterogeneous integration for on-chip quantum photonic circuits with single quantum dot devices,” *Nat. Commun.* **8**, 889 (2017).
- <sup>18</sup>A. Chanana *et al.*, “Ultra-low loss quantum photonic circuits integrated with single quantum emitters,” *Nat. Commun.* **13**, 7693 (2022).
- <sup>19</sup>S. L. Mouradian *et al.*, “Scalable integration of long-lived quantum memories into a photonic circuit,” *Phys. Rev. X* **5**, 031009 (2015).
- <sup>20</sup>N. H. Wan *et al.*, “Large-scale integration of artificial atoms in hybrid photonic circuits,” *Nature* **583**, 226 (2020).
- <sup>21</sup>S. Kim, N. M. H. Duong, M. Nguyen, T. J. Lu, M. Kianinia, N. Mendelson, A. Solntsev, C. Bradac, D. R. Englund, and I. Aharonovich, “Integrated on chip platform with quantum emitters in layered materials,” *Adv. Opt. Mater.* **7**, 1901132 (2019).
- <sup>22</sup>A. W. Elshaari, A. Skalli, S. Gyger, M. Nurizzo, L. Schweickert, I. Esmaeil Zadeh, M. Svedendahl, S. Steinhauer, and V. Zwiller, “Deterministic integration of HBN emitter in silicon nitride photonic waveguide,” *Adv. Quantum Technol.* **4**, 2100032 (2021).
- <sup>23</sup>K. Parto, S. I. Azzam, N. Lewis, S. D. Patel, S. Umezawa, K. Watanabe, T. Taniguchi, and G. Moody, “Cavity-enhanced 2D material quantum emitters deterministically integrated with silicon nitride microresonators,” *Nano Lett.* **22**, 9748 (2022).
- <sup>24</sup>S. Bogdanov, M. Y. Shalaginov, A. Boltasseva, and V. M. Shalaev, “Material platforms for integrated quantum photonics,” *Opt. Mater. Express* **7**, 111 (2017).
- <sup>25</sup>A. W. Elshaari, W. Pernice, K. Srinivasan, O. Benson, and V. Zwiller, “Hybrid integrated quantum photonic circuits,” *Nat. Photonics* **14**, 285 (2020).
- <sup>26</sup>J. Kim, S. Aghaeimeibodi, J. Carolan, D. Englund, and E. Waks, “Hybrid integration methods for on-chip quantum photonics,” *Optica* **7**, 291 (2020).
- <sup>27</sup>W. Redjem *et al.*, “Single artificial atoms in silicon emitting at telecom wavelengths,” *Nat. Electron.* **3**, 738 (2020).
- <sup>28</sup>M. Prabhu, C. Errando-Herranz, L. De Santis, I. Christen, C. Chen, C. Gerlach, and D. Englund, “Individually addressable and spectrally programmable artificial atoms in silicon photonics,” *Nat. Commun.* **14**, 2380 (2023).
- <sup>29</sup>W. Redjem *et al.*, “All-silicon quantum light source by embedding an atomic emissive center in a nanophotonic cavity,” *Nat. Commun.* **14**, 3321 (2023).
- <sup>30</sup>D. M. Lukin, M. A. Guidry, and J. Vučković, “Integrated quantum photonics with silicon carbide: Challenges and prospects,” *PRX Quantum* **1**, 020102 (2020).
- <sup>31</sup>D. M. Lukin *et al.*, “4H-silicon-carbide-on-insulator for integrated quantum and nonlinear photonics,” *Nat. Photonics* **14**, 330 (2020).
- <sup>32</sup>S. Castelletto, S. Rodt, and S. Reitzenstein, “Silicon carbide single-photon sources: Challenges and prospects,” *Mater. Quantum Technol.* **1**, 023001 (2021).
- <sup>33</sup>A. Senichev, Z. O. Martin, S. Peana, D. Sychev, X. Xu, A. S. Lagutchev, A. Boltasseva, and V. M. Shalaev, “Room-temperature single-photon emitters in silicon nitride,” *Sci. Adv.* **7**, FW41.6 (2021).
- <sup>34</sup>A. Senichev, S. Peana, Z. O. Martin, O. Yesilyurt, D. Sychev, A. S. Lagutchev, A. Boltasseva, and V. M. Shalaev, “Silicon nitride waveguides with intrinsic single-photon emitters for integrated quantum photonics,” *ACS Photonics* **9**, 3357 (2022).
- <sup>35</sup>Z. O. Martin, A. Senichev, S. Peana, B. J. Lawrie, A. S. Lagutchev, A. Boltasseva, and V. M. Shalaev, “Photophysics of intrinsic single-photon emitters in silicon nitride at low temperatures,” *Adv. Quantum Technol.* **6**, 2300099 (2023).
- <sup>36</sup>Y. Xue *et al.*, “Single-photon emission from point defects in aluminum nitride films,” *J. Phys. Chem. Lett.* **11**, 2689 (2020).
- <sup>37</sup>S. G. Bishop, J. P. Hadden, F. Alzahrani, R. Hekmati, D. L. Huffaker, W. W. Langbein, and A. J. Bennett, “Room temperature quantum emitter in aluminum nitride,” *ACS Photonics* **7**, 1636 (2020).
- <sup>38</sup>T.-J. Lu, B. Lienhard, K.-Y. Jeong, H. Moon, A. Iranmanesh, G. Grosso, and D. Englund, “Bright high-purity quantum emitters in aluminum nitride integrated photonics,” *ACS Photonics* **7**, 2650 (2020).
- <sup>39</sup>A. M. Berhane *et al.*, “Bright room-temperature single-photon emission from defects in gallium nitride,” *Adv. Mater.* **29**, 1605092 (2017).
- <sup>40</sup>A. M. Berhane, K.-Y. Y. Jeong, C. Bradac, M. Walsh, D. Englund, M. Toth, and I. Aharonovich, “Photophysics of GaN single-photon emitters in the visible spectral range,” *Phys. Rev. B* **97**, 165202 (2018).
- <sup>41</sup>Y. Zhou, Z. Wang, A. Rasmita, S. Kim, A. Berhane, Z. Bodrog, G. Adamo, A. Gali, I. Aharonovich, and W. B. Gao, “Room temperature solid-state quantum emitters in the telecom range,” *Sci. Adv.* **4**, eaar3580 (2018).
- <sup>42</sup>W. H. P. Pernice, C. Xiong, C. Schuck, and H. X. Tang, “Second harmonic generation in phase matched aluminum nitride waveguides and micro-ring resonators,” *Appl. Phys. Lett.* **100**, 223501 (2012).
- <sup>43</sup>C. Wang, M. J. Burek, Z. Lin, H. A. Atikian, V. Venkataraman, C. Huang, P. Stark, and M. Lončar, “Integrated high quality factor lithium niobate microdisk resonators,” *Opt. Express* **22**, 30924 (2014).
- <sup>44</sup>S. Zhu, Q. Zhong, T. Hu, Y. Li, Z. Xu, Y. Dong, and N. Singh, “Aluminum nitride ultralow loss waveguides and push-pull electro-optic modulators for near infrared and visible integrated photonics,” *Optical Fiber Communication Conference (OFC) 2019, OSA Technical Digest* (Optica Publishing Group, 2019) paper W2A.11 (2019).
- <sup>45</sup>J. Liu, G. Huang, R. N. Wang, J. He, A. S. Raja, T. Liu, N. J. Engelsen, and T. J. Kippenberg, “High-yield, wafer-scale fabrication of ultralow-loss, dispersion-engineered silicon nitride photonic circuits,” *Nat. Commun.* **12**, 2236 (2021).
- <sup>46</sup>T.-J. Lu *et al.*, “Aluminum nitride integrated photonics platform for the ultraviolet to visible spectrum,” *Opt. Express* **26**, 11147 (2018).
- <sup>47</sup>N. Li, C. P. Ho, S. Zhu, Y. H. Fu, Y. Zhu, and L. Y. T. Lee, “Aluminium nitride integrated photonics: A review,” *Nanophotonics* **10**, 2347 (2021).
- <sup>48</sup>M. Dong, G. Clark, A. J. Leenheer, M. Zimmermann, D. Dominguez, A. J. Menssen, D. Heim, G. Gilbert, D. Englund, and M. Eichenfield, “High-speed programmable photonic circuits in a cryogenically compatible, visible-NIR 200 mm CMOS architecture,” *Nat. Photon.* **16**, 59 (2022).
- <sup>49</sup>X. Liu, A. W. Bruch, and H. X. Tang, “Aluminum nitride photonic integrated circuits: From piezo-optomechanics to nonlinear optics,” *Adv. Opt. Photonics* **15**, 236 (2023).
- <sup>50</sup>Y. Xue, T. Wei, H. Chang, D. Liang, X. Dou, and B. Sun, “Experimental optical properties of single-photon emitters in aluminum nitride films,” *J. Phys. Chem. C* **125**, 11043 (2021).
- <sup>51</sup>X. Wang *et al.*, “Quantum emitters with narrow band and high Debye–Waller factor in aluminum nitride written by femtosecond laser,” *Nano Lett.* **23**, 2743 (2023).
- <sup>52</sup>J. B. Varley, A. Janotti, and C. G. Van De Walle, “Defects in AlN as candidates for solid-state qubits,” *Phys. Rev. B* **93**, 161201 (2016).
- <sup>53</sup>H. Seo, M. Govoni, and G. Galli, “Design of defect spins in piezoelectric aluminum nitride for solid-state hybrid quantum technologies,” *Sci. Rep.* **6**, 20803 (2016).
- <sup>54</sup>A. Aghdaei, R. Pandiyan, B. Ilahi, M. Chicoine, M. El Gowini, F. Schiettekatte, L. G. Fréchet, and D. Morris, “Engineering visible light emitting point defects in Zr-implanted polycrystalline AlN films,” *J. Appl. Phys.* **128**, 245701 (2020).
- <sup>55</sup>H. Fiedler, V. Jovic, D. R. G. Mitchell, J. Leveueur, E. Anquillare, K. E. Smith, and J. Kennedy, “Tuning the electromechanical properties and polarization of aluminium nitride by ion beam-induced point defects,” *Acta Mater.* **203**, 116495 (2021).
- <sup>56</sup>H. Fiedler, J. Leveueur, D. R. G. Mitchell, S. Arulkumaran, G. I. Ng, A. Alphones, and J. Kennedy, “Enhancing the piezoelectric modulus of wurtzite AlN by ion beam strain engineering,” *Appl. Phys. Lett.* **118**, 012108 (2021).
- <sup>57</sup>E. N. Hernández, H. B. Ya, V. Pugliese, P. Aprà, J. K. Cannon, S. G. Bishop *et al.*, “Fabrication of quantum emitters in aluminium nitride by Al-ion implantation and thermal annealing,” *Appl. Phys. Lett.* **124**, 124003 (2024).